Freestanding MXene-MnO_2 films for Li-CO_2 cathodes with low overpotential and long-term cycling.

WANG, Y., WANG, X., GE, B., GUO, J., FERNANDEZ, C. and PENG, Q.

2021

Freestanding MXene–MnO_2 Films for Li–CO_2 Cathodes with Low Overpotential and Long-Term Cycling

Yangyang Wang[1], Xue Wang[1], Bingcheng Ge[1], Jianxin Guo[2], Carlos Fernandez[3], and Qiuming Peng[1]*

[1]CENC, State Key Laboratory of Metastable Materials Science and Technology, Yanshan University, Qinhuangdao 066004, China.

[2] Hebei Provincial Key Lab of Optoelectronic Information Materials, College of Physics Science and Technology, Hebei University, Baoding 071002, China.

[3] School of Pharmacy and Life Sciences, Robert Gordon University, Aberdeen AB107GJ, U.K.

Corresponding Author - Qiuming Peng; Email: pengqiuming@ysu.edu.cn

Abstract

The Li–CO_2 battery is a potential energy storage device that not only possesses a theoretical energy density as high as 1876 W h kg^{-1} but also alleviates the consumption of fossil resources by converting the greenhouse gas CO_2 into electric energy. However, some technique bottlenecks, such as high overpotential, low recyclability, and low energy density, severely prohibit its application rhythm. Here, we prepare a binder-free MXene–MnO_2 composite film using vacuum-assisted filtration and in situ reduction, which can be used as a freestanding cathode for Li–CO_2 batteries. This MXene–MnO_2 film electrode bestows good cycle stability (~220 cycles), high specific capacity, and lower overpotential (~0.89 V) in Li–CO_2 batteries. Both experimental tests and first-principles calculations reveal that the enhanced electrochemical properties are associated with three aspects. First, the MXene–MnO_2 film offers a high electrical conductivity and porous structure, which provide fast transport channels for electrons and ions. Then, the replacement of Mn by Ti increases the adsorption of Li ions, which facilitates the rapid decomposition of Li_2CO_3. Finally, the synergistic effect of MXene and MnO_2 exposes a large number of active sites, which increases the capacity of Li–CO_2 batteries. Therefore, this self-supporting strategy on the MXene composite paves a way to develop high-performance Li–CO_2 batteries.

KEYWORDS: Li–CO_2 batteries catalyst cycle stability MXene−MnO_2 film freestanding cathode

1. Introduction

With increasing demand of high-energy density devices, traditional Li-ion batteries are unable to meet the demands of the transport electrification and large-scale grid energy storage.[1−3] Metal–air batteries, due to their unique merits such as high operating voltage and large capacity, have attracted great research attention.[4] Among them, Li–CO_2 batteries have been considered as a new type of energy storage device, with special interest to reduce CO_2 emissions. However, their poor rechargeability and low application current density prohibit the applications. The reversible electrochemical reaction of $4Li + 3CO_2 \leftrightarrow 2Li_2CO_3 + C$ (E_0 = 2.8 V *vs* Li/Li+)[5,6] can theoretically release a high energy density of 1876 W h kg^{-1}.[5,7−9] Metal Li is oxidized at the anode during the discharge process, wherein Li ions are released into the electrolyte, while CO_2 gas is reduced at the cathode to

generate carbonate (CO_3^{2-}) anions and amorphous carbon. Therefore, the reversible formation/decomposition of discharge products (Li_2CO_3) is an important process in Li–CO_2 batteries. The discharge product Li_2CO_3 is a wide-band gap insulator with low conductivity, slow decomposition kinetics, and poor thermodynamic stability,[10] and thus, a high charging voltage is required to completely decompose Li_2CO_3 during the charging process. However, excessively high overpotential also leads to electrolyte decomposition, which shortens the cycle stability and lifetime of Li–CO_2 batteries.

Noble metal-based catalysts[5,11−13] have shown low overpotential and high cycling stability, yet the unaffordable cost has hindered their widespread application. Alternatively, transition-metal oxides (TMOs)[14] have gained tremendous attention due to their excellent catalytic properties. For instance, the NiO–CNT composition served as an effective cathode for the Li–CO_2 battery with high coulombic stability and good circulation stabilization.[15] The Li–CO_2 batteries with $ZnCo_2O_4$@CNT cathode exhibited a full load discharge capacity of 4275 mA h g^{-1} and excellent cycling performance.[16] However, some discharge intermediates often result in the premature cell mortality. Moreover, the catalytic performance is also restricted by the high resistance of TMOs. Accordingly, there is an imperative need to develop highly conductive and structure-stabilized TMO-based catalysts.

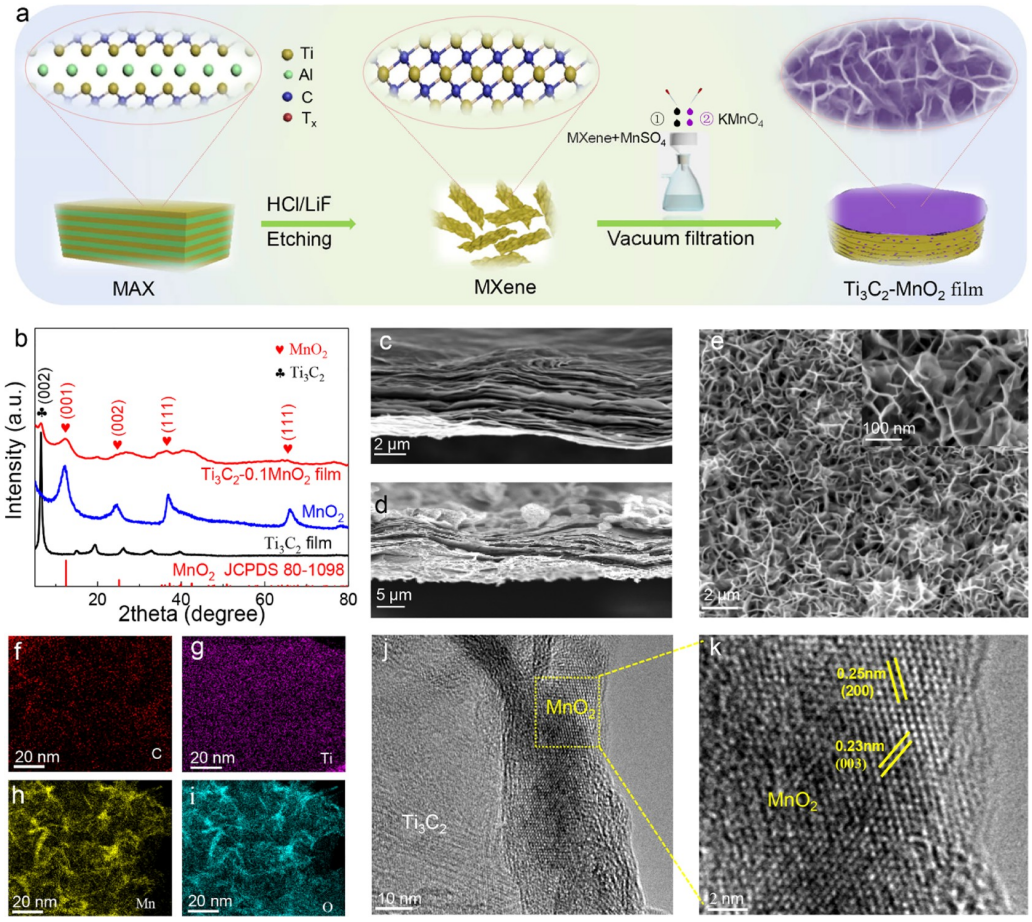

Figure 1. (a) Schematic diagram of the synthesis of Ti_3C_2–MnO_2 films. Microstructural characteristics: (b) XRD patterns of the Ti_3C_2 film, MnO_2, and Ti_3C_2–0.1MnO_2 film. (c,d) Cross-sectional SEM image of the Ti_3C_2 film and Ti_3C_2–0.1MnO_2 film. (e) Top-view SEM image of the Ti_3C_2–0.1MnO_2 film. The inset corresponds to its local high-magnification image. (f–i) Corresponding elemental distribution, (j) TEM image, and (k) HRTEM image of the Ti_3C_2–0.1MnO_2 film, respectively.

MXenes are novel two-dimensional nanomaterials derived from a large family of transition-metal carbides, nitrides, and carbon-nitrides and allow for excellent electrical conductivity and efficient charge transportation,[17] due to abundant exposed metal sites.[18] These attractive properties make MXenes potential candidates for energy storage and conversion.[19–25] Notably, MXenes promote rapid electron transfer to electrochemically active sites, facilitating facile electrochemical reactions.[19] In addition, MXene can also act as a strong support to prevent structural variation during the electrochemical reaction of TMOs.[26] Among the MXenes, Ti_3C_2Tx is particularly notable for high capacitance (≈1500 F cm^{-3})[27] in combination with good conductivity (≈15,000 S cm^{-1}).[27,28]
Herein, a new flexible, binder-free MXene–MnO_2 combination was prepared as a cathode catalyst for Li–CO_2 batteries by vacuum-assisted filtration and in situ reduction. The synergic effect between MXene and MnO_2 enables the Li–CO_2 battery to perform good cycling stability (∼220 cycles), higher specific capacity, and lower overpotential (∼0.89 V), compared with single MXene film or MnO_2 cathode catalyst. This work paves the way to design a self-supporting cathode catalyst in Li–CO_2 batteries, contributing to the development of high-performance Li–CO_2 batteries.

2. Experimental Section

Ti_3AlC_2 (500 mesh) was bought from Laizhou Kai Kai Ceramic Materials Co., Ltd. LiF (99.99%) was bought from Aladdin Reagent (Shanghai) Co., Ltd., China. Delaminated Ti_3C_2Tx suspension was attained via in situ etching Ti_3AlC_2 powders using LiF/HCl. Specifically, 1.6 g of LiF was added into a Teflon beaker (50 mL) with 20 mL of 9 M HCl under continuous stirring.
Then, 1.0 g of Ti_3AlC_2 powder was slowly added into the mixture solution and maintained at 40 °C for 48 h. The resultant solid residue was washed with deionized water by repeated centrifugation until the pH was above 6. Then, the precipitate was diluted to 200 mL of deionized water and bath sonicated in ice for 1 h. Finally, the solution was centrifuged at 3500 rpm to collect the single or few-layered MXene dispersion. The concentration of this suspension was 2 mg mL^{-1}. Fabrication of Ti_3C_2–MnO_2 films: 20 mL of 1.4 mM $MnSO_4{\cdot}H_2O$ was added into 20 mL of the aforementioned MXene suspension and stirred for 1 h. Subsequently, 40 mL of the above-synthesized mixture was prepared using vacuum-assisted filtration through a PVDF membrane. 20 mL of $KMnO_4$ (1.6 mM) aqueous solution was quickly added into the vacuum-assisted filtration. Finally, the freestanding Ti_3C_2–MnO_2 film sediment was stored by freeze drying for 48 h. Different Ti_3C_2/$MnSO_4$ molar ratios of 1:0.05, 1:0.1, and 1:0.2 in the initial solutions were prepared, and the products were designated as the Ti_3C_2–0.05MnO_2 film, Ti_3C_2–0.1MnO_2 film, and Ti_3C_2–0.2MnO_2 film, respectively. The Ti_3C_2 film and MnO_2 were synthesized in the same way as mentioned above, except that MnO_2 or MXene was not added.

2.2. Material Characterization

The crystal structure of the samples was analyzed on an X-ray diffractometer (Rigaku D/Max-2005/PC), which used Cu Kα radiation (λ = 1.5406 Å) with a scan rate of 2°/min. Scanning electron microscopy (SEM) was conducted with a Hitachi S-4800. Transmission electron microscopy (TEM) measurements were taken using a Titan ETEM G2 at 300 kV. The specific surface area and pore size profiles of the samples were investigated by nitrogen adsorption at 77 K (−196 °C) by a Micromeritics ASAP2020. X-ray photoelectron spectroscopy (XPS) illustrations were examined with Al Kα (1486.71 eV) X-ray radiation (15 kV and 10 mA) on a Thermo Fisher instrument. The binding energies derived in the XPS analysis were adjusted by referencing the C 1s peak position (284.80 eV).

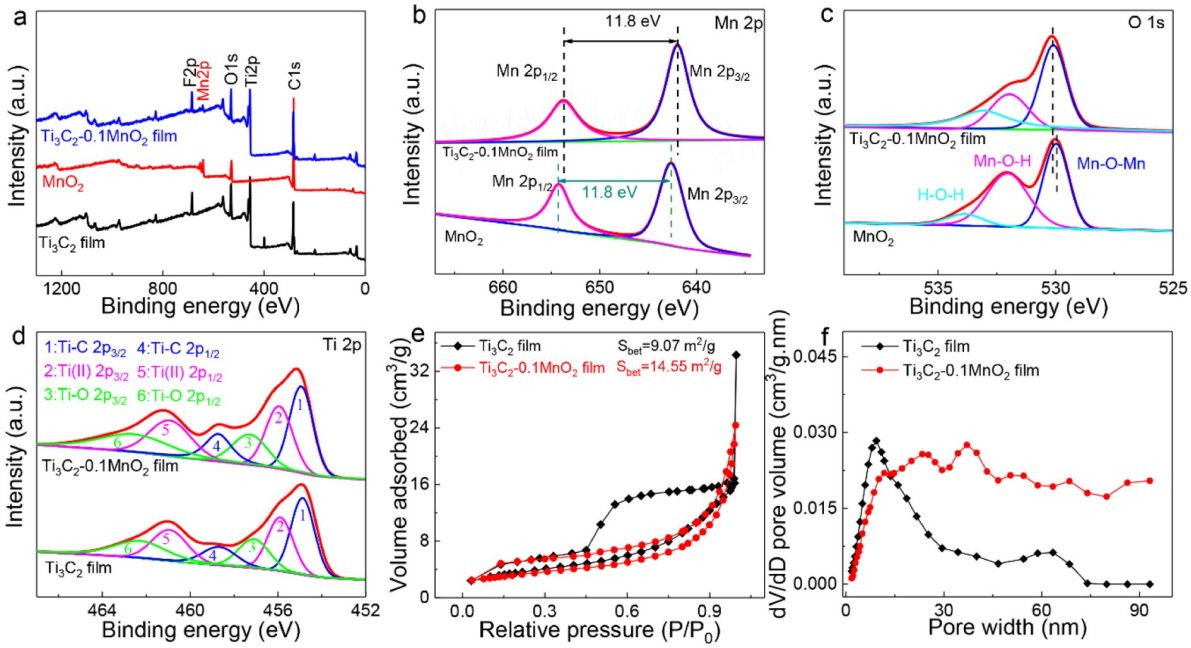

Figure 2. (a) XPS survey spectra of the Ti_3C_2 film, MnO_2, and Ti_3C_2–0.1MnO_2 film. (b–d) XPS profiles of Mn 2p, O 1s, and Ti 2p, respectively. (e) N2 adsorption–desorption isotherms and (f) aperture distribution profile of the Ti_3C_2 film and Ti_3C_2–0.1MnO_2 film.

2.3. Electrochemical Measurements

Due to the low capacity of the Ti_3C_2 film-based Li–CO_2 battery, the electrical current density and specific gravity capacity of all electrodes are derived from the mass of manganese dioxide. The mass loading of the Ti_3C_2–MnO_2 film was found to be 0.5–0.7 mg cm^{-2}. The Li–CO_2 batteries, based on a CR2032 coin-type battery, were assembled in a glovebox filled with argon with an ambient level of water and oxygen of less than 0.1 ppm. They were made up of a lithium foil anode (14 mm in diam), a glass fiber filter separator (16 mm in diam), an electrolyte (1 M LiTFSI dissolved in TEGDME solution), and an air cathode.

The freestanding Ti_3C_2–MnO_2 film cathodes were cut into disks (12 mm diam). A hole (4 mm in diam) was tapped into the cathode casing so that carbon dioxide could easily and quickly access the cathode. The assembled cell was then kept in a 250 mL glass container fully filled with high purity carbon dioxide. The pure carbon dioxide is pumped into the glass vessel via a direct bi-directional piston, which is alternately evacuated and vented three times. After 10 h incubation, the cells were tested for charge/discharge cycles. For all Li–CO_2 cells, 1 M LiTFSI dissolved in TEGDME solution was chosen as the electrolyte. All potentials were compared to Li/Li^+. The constant current discharge/charge tests are carried out on the LAND CT2001A battery tester. Cyclic voltammetry (CVs) and electrochemical impedance spectroscopy (EIS) curves were performed at the BioLogic VMP_3 system.

2.4. Calculations

In density functional theory (DFT) simulations,[29,30] the Vienna ab initio Simulation Package (VASP)[31] was used for geometric optimization and reaction process imitation. Nuclear electrons are denoted by the enhanced wave potential of the emission. We employed generalized gradient approximation with the Perdew–Wang functional (PW91)[32] to describe exchange and correlation effects. The dynamic power cut-off is 500 eV. The K-point sampling is 7 × 5 × 1. The structure was selected for the

optimization with a force convergence criterion of 0.01 eV/Å and an energy convergence criterion of 10^{-6} eV. The optimized lattice constant of δ-MnO_2 is $a = b = 0.29$ nm, $c = 0.51$ nm.

3. Results and Discussion

3.1. Characterization of MXene–MnO_2 Films

A freestanding, binder-free MXene–MnO_2 film is prepared through a vacuum filtering method and redox reaction (precise steps are shown in the experimental section). As depicted in Figure 1a, the Al layers in the pristine bulk Ti_3AlC_2 MAX were selectively removed by etching with mixed LiF/HCl solution. Subsequently, the MXene–MnO_2 film was formed by in situ reduction. The X-ray diffraction (XRD) patterns (Figures 1b and S1a) show that the strong characteristic peak of (002) for the MXene film is moved to a lower angle ($2\theta \approx 6.5°$). Meanwhile, the peak at ∼39°, corresponding to the (104) plane of Ti_3AlC_2 (SEM Figure S1b), disappeared, which suggests that the Al layers are successfully etched from the MAX phase, and the MXene structure is formed (Figure S2).[33] All peaks in the pattern of MnO_2 are notably indexed to the δ-MnO_2 (JCPDS no. 80-1098), and they remained in the Ti_3C_2–$0.1MnO_2$ film. The cross-sectional (Figure 1c) and top view (Figure S2b) SEM images of bare Ti_3C_2 film indicate that the well-dispersed few-layer MXene nanosheets can be achieved by simple vacuum filtration. The optical photographs of the curving Ti_3C_2Tx MXene film and the Tyndall effect of laser irradiation (Figure S4a) exhibit excellent flexibility and dispersibility. After vacuum filtration and redox reaction, the MnO_2 nanosheets are uniformly loaded on the Ti_3C_2 film and have a larger specific surface area and better electrical conductivity, as evidenced in Figure 1d (cross-sectional SEM), Figure 1e (top-view SEM), and Figure S4b (optical photographs), compared with separate MnO_2 (Figure S3). The elemental mappings (Figure 1f–i) result with homogeneous C, Ti, O, and Mn distribution in MXene–MnO_2 films, which is also consistent with the easy conglutination between MnO_2 nanosheets and MXene substrates (Figure S5a,b). Additionally, as shown in the high-resolution TEM (HRTEM) image (Figure 1j,k), the lattice spacing of 0.25 and 0.23 nm is assigned to the (200) and (003) planes of the MnO_2, respectively. Finally, the selected area electron diffraction (SAED) pattern (Figure S5c) clearly shows the coexistence of Ti_3C_2 films and MnO_2 nanosheets. As a comparison, different concentrations of MnO_2 grown in situ on MXene were prepared, and they are termed as Ti_3C_2–$0.05MnO_2$ and Ti_3C_2–$0.2MnO_2$ films, respectively. The morphology of MnO_2 varies depending on the concentration, as shown in Figures S6 and S7.

In addition, as assessed by XPS (Figure 2a), the characteristic peaks of Ti 2p, O 1s, C 1s, F 1s, and Mn 2p are observed, indicating the appearance of these ingredients in the combination. In the Mn 2p fine spectrum (Figure 2b), the splitting energy from the Mn 2p of MnO_2 to that of the Ti_3C_2–$0.1MnO_2$ film is 11.8 eV.[34] Moreover, the overall binding energy of the Ti_3C_2–$0.1MnO_2$ film shifts to a lower binding energy, owing to electron transfer between the functional groups of the MXene surface and MnO_2. On the other hand, since Ti occupies the active site of Mn, the O 1s fine spectrum of the Ti_3C_2–$0.1MnO_2$ film (Figure 2c) moves slightly to the direction of high binding energy. Consistently, the Ti 2p fine spectra have almost unchanged before and after reaction (Figure 2d). This phenomenon has occurred in our previous work.[35] The variation of specific surface area and pore size is further investigated by the Brunauer–Emmett–Teller (BET) test. Basically, compared with the pristine Ti_3C_2 film (9.07 m2/g), the formed Ti_3C_2–$0.1MnO_2$ film composite material sample has the larger BET surface area of 14.55 m2/g (Figure 2e), offering more active sites for CO_2 in the charging and discharging processes than other counterparts. More importantly, the Ti_3C_2–$0.1MnO_2$ film has larger coarse pores which facilitate ion and electron transportation, as shown in Figure 2f.

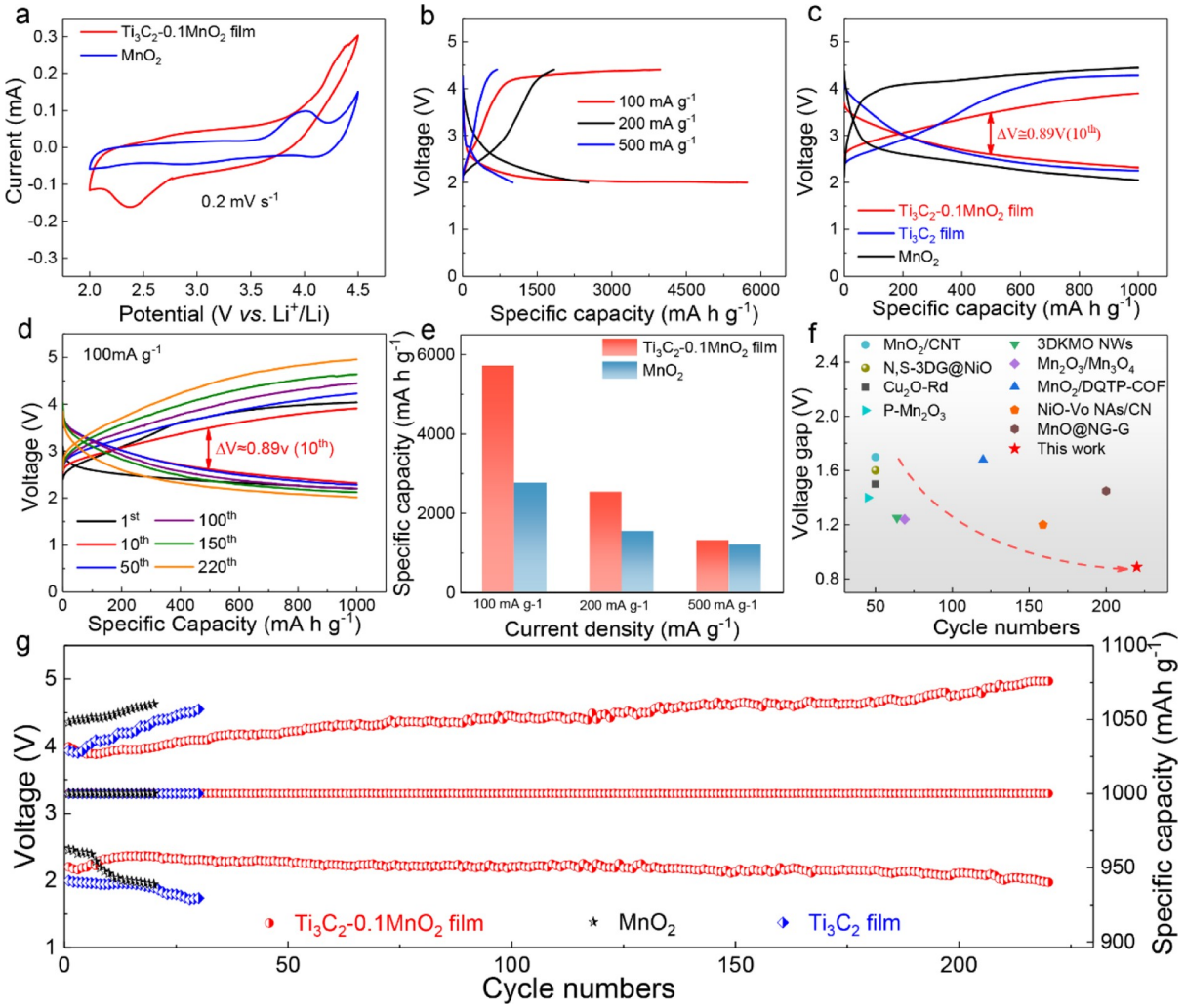

Figure 3. (a) CV curves of the Ti_3C_2–0.1MnO_2 film and MnO_2 under CO_2-saturated conditions. (b) Full discharge–charge profiles of Ti_3C_2–0.1MnO_2 films under 100, 200, and 500 mA g^{-1}, respectively. (c) First discharge–charge curves under a current density of 100 mA g^{-1} and a specific capacity of 1000 mA h g^{-1} with three different cathodes. (d) Discharge–charge curves of the Ti_3C_2–0.1MnO_2 film. (e) Charge–discharge curves of the full capacity with Ti_3C_2–0.1MnO_2 films and MnO_2 cathodes at different current densities. (f) Comparison of recycling behavior and charging/discharging voltage range among the Mn oxide-based materials as cathodes for Li–CO_2 battery literature surveyed. (g) Terminal discharge voltage profiles during cycling of Ti_3C_2–0.1MnO_2 films, MnO_2, Ti_3C_2 film-based Li–CO_2 batteries.

3.2. Electrochemical Properties

CV curves were determined at a scan rate of 0.2 mV $^{s-1}$ with Li/Li^+ in the range of 2–4.5 V at high purity CO2 (Figure 3a). Compared with those of the pure MnO_2 cathode, the Ti_3C_2–0.1MnO_2 film cathode performs a higher CO_2 reduction reaction onset potential (CO_2RR, ≈2.36 V) and a lower CO_2 evolution reaction onset potential (CO_2ER, ≈3.8 V).[5] The results show that the Ti_3C_2–0.1MnO_2 film electrode is beneficial for both the formation and decomposition of Li_2CO_3 in Li–CO_2 batteries. Figure 3b shows the voltage distribution of the flexible, binder-free Ti_3C_2–0.1MnO_2 film cathode in Li–CO_2 batteries at different current densities. Under CO_2 conditions, the batteries have a capacity of 5722, 2525, and 1007 mA h g^{-1} at current densities of 100, 200, and 500 mA g^{-1}, respectively. When the

discharge/charge capacity is limited to 1000 mA h g^{-1} at a current density of 100 mA g^{-1}, as shown in Figure 3c, the Ti_3C_2–0.1MnO_2 film cathode exhibits low polarization with a discharge overcharge potential of 0.89 V in the tenth cycle. On the contrary, the overpotential adds up to 1.33 V for the Ti_3C_2 film and 1.87 V for MnO_2, respectively. The cycling performance of the Ti_3C_2–0.1MnO_2 film electrode was examined to evaluate its electrocatalytic activity and stability. Figure 3d shows that the Li–CO_2 batteries with Ti_3C_2–0.1MnO_2 film electrode exhibit stable and reversible cycling over 220 cycles at 100 mA g^{-1}. They are able to withstand 180 (Figure S8a,b) and 60 (Figure S8d,e) cycles when the electrical current density is 200 and 500 mA g^{-1}, respectively. Furthermore, the Ti_3C_2–0.05MnO_2 film, Ti_3C_2–0.2MnO_2 film, pure MXene film, and MnO_2 electrode were also tested under the same conditions, and they only show 50 (Figure S9a,b), 60 (Figure S9d,e), 30 (Figure S10a,b), and 20 (Figure S11a,b) cycles, respectively, which demonstrates the best catalytic activity and cycling stability than that of the Ti_3C_2–0.1MnO_2 film. Moreover, the Ti_3C_2–0.1MnO_2 film cathode delivers a higher discharge capacity at 100 mA g^{-1}, while those of MnO_2-based cathodes are only 2757 mA h g^{-1} (Figure 3e). As summarized in Figure 3f, the recycling behavior of Li–CO_2 batteries with the Ti_3C_2–0.1MnO_2 film cathode is the best among the Mn oxide-based materials, as cathodes for Li–CO_2 battery literature surveyed.(36−44) In addition, the specific capacities of the first five turns of the Ti_3C_2–0.1MnO_2 film cathode catalyst for current densities of 200 and 500 mA g^{-1} are shown in Figure S8c,f, respectively. Figure 3g presents the cycling galvanostatic discharge/recharge curves of the hybrid Ti_3C_2–0.1MnO_2 film cathode with the fixed capacity of 1000 mA h g^{-1} at a current density of 100 mA g^{-1}, and it maintains a stable terminal discharge voltage above 2.0 V after 220 cycles. Furthermore, a concrete comparison of the cycle numbers for the five different sample-equipped electrodes in Li–CO_2 batteries is shown in Figure S12.

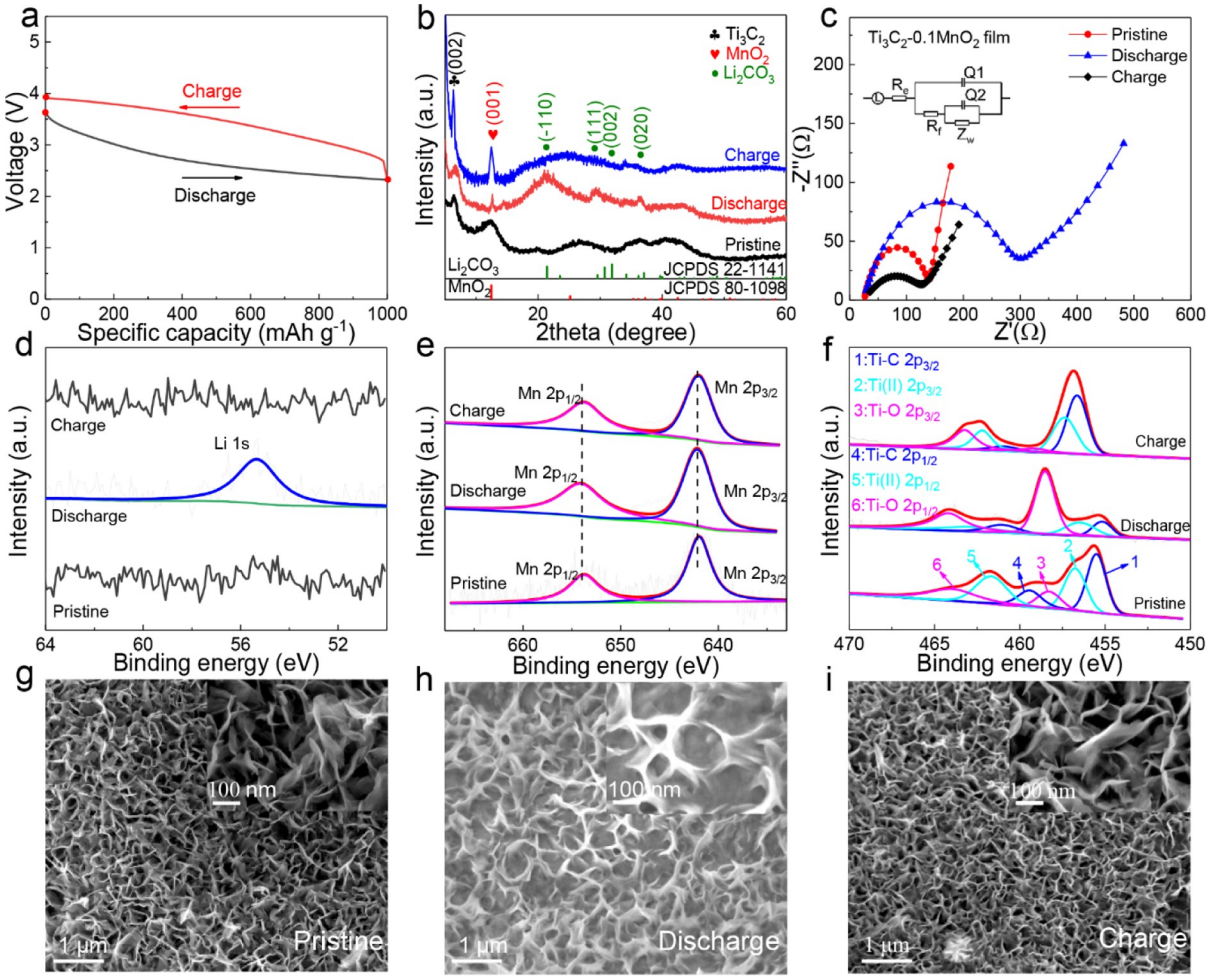

Figure 4. (a) Preliminary circular electrostatic discharging/charging characteristics. (b) XRD patterns of the Ti_3C_2–0.1MnO_2 film-based cathode in different states. (c) EIS about Ti_3C_2–0.1MnO_2 films in different states. (d–f) XPS profiles of Li 1s, Mn 2p, and Ti 2p in different states, respectively. SEM images of the Ti_3C_2–0.1MnO_2 film-based cathode in different stages: (g) before discharge, (h) after discharge, and (i) after recharge.

3.3. Reaction Mechanism

Figure 4a shows preliminary circular electrostatic discharging/charging characteristic with the Ti_3C_2–0.1MnO_2 film as the cathode at a current density of 100 mA g^{-1}. As shown in Figure 4b, the typical peaks of Li_2CO_3 (JCPDS no. 22-1141) can be easily detected in the discharging Li–CO_2 battery with the Ti_3C_2–0.1MnO_2 film cathode. However, after charging, the characteristic peak of Li_2CO_3 disappears, suggesting the complete decomposition of the discharge product. In addition, the reversible formation/decomposition of Li_2CO_3 is further verified by Fourier-transform infrared (Figure S13). Figure 4c shows the EIS spectrum of the Ti_3C_2–0.1MnO_2 film electrode during the charging and discharging cycles at 100 mA g^{-1}. Compared with the pristine electrode, a larger semicircle appears in the discharged state, indicating that the precipitation of the insulating discharging product Li_2CO_3 on the surface of the Ti_3C_2–0.1MnO_2 film electrode leads to a significant increase in impedance. However, the pristine interface (high-frequency part), charge transfer (high-middle frequency region), and diffusion resistance (straight line) can be recovered to a large extent during the subsequent charging process. EIS plots (Figure S14a–d) and fitting parameters of EIS curves (Tables S1–S3) uncover that the

Ti_3C_2–0.1MnO_2 film has the smallest value of surface film resistance (Rf) and charge-transfer resistance (R_{ct}) among the samples considered, proving its good conductivity at the same time.
XPS spectrum of Li 1s (Figure 4d) for the discharged Ti_3C_2–0.1MnO_2 film shows a characteristic peak at 55.2 eV, assigned to Li_2CO_3, which then disappears after the full recharge process, verifying the complete decomposition of Li_2CO_3 and the high reversibility of the Li–CO_2 battery. The fine spectrum of Mn 2p (Figure 4e) shows that the binding energy of Mn 2p is maintained during the charging and discharging process, which demonstrates the superior stability of the Ti_3C_2–0.1MnO_2 film during the cycle of the Li–CO_2 cell. Interestingly, the fine spectrum of Ti 2p (Figure 4f) during the charge/recharge process changes a little, which might be associated with electron transfer from Ti to Mn. The SEM image shows that the surface of pristine Ti_3C_2–0.1MnO_2 film is smooth and clean (Figure 4g). However, the discharge product Li_2CO_3, like a paste, is uniformly deposited on the catalyst surface after discharging (Figures 4h and S15a). Moreover, the surface morphology of the cathode catalyst returns to its original state (Figures 4i and S15b,c), which demonstrates the good reversibility and stability of the Ti_3C_2–0.1MnO_2 film as a catalyst.

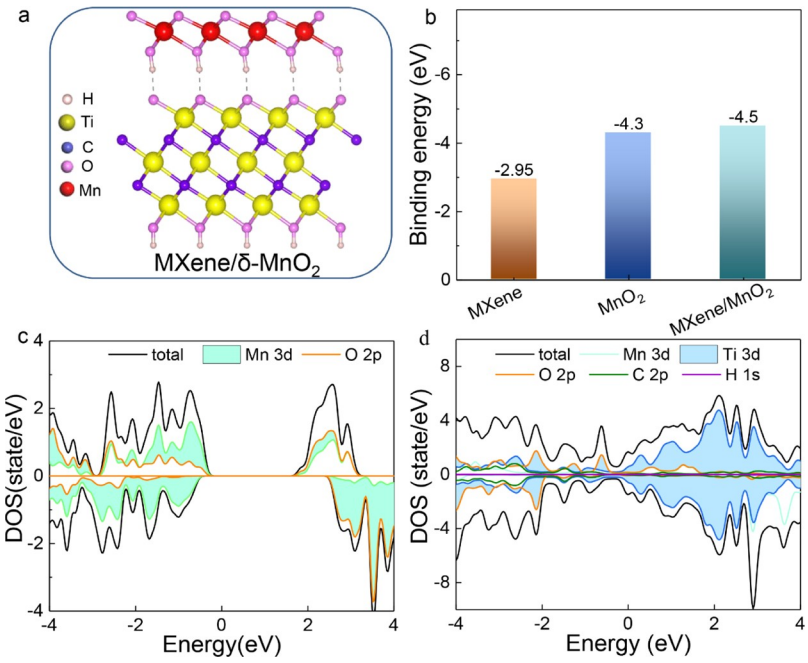

Figure 5. Theoretical calculations. Schematic model for adsorption of lithium in (a) Ti_3C_2 (001), $Ti_{3-x}Mn_xC_2$ (001), $Ti_3C_2O_2$ (001), and $Ti_{3-x}Mn_xC_2O_2$ (001), respectively. (b) Adsorption energy of lithium in Ti_3C_2 (001), $Ti_{3-x}Mn_xC_2$ (001), $Ti_3C_2O_2$ (001), and $Ti_{3-x}Mn_xC_2O_2$ (001), respectively. The DOS of (c) MnO_2 and (d) Ti_3C_2–MnO_2 films, respectively.

To clarify the mechanism of the electrocatalytic activity of the Ti_3C_2–0.1MnO_2 film cathode, DFT calculations have been performed. Crystal texture and band structures of δ-MnO_2 and MXene/δ-MnO_2 are shown in Figures 5a and S16. According to the structure, the MnO_2 lamellar gap is a tetrahedral gap, which becomes an octahedral gap in MXene/δ-MnO_2 after in situ growth on MXene. Simultaneously, the H atoms in the functional group of MXene combine with the O atoms in MnO_2. Moreover, Figure 5b discloses that the adsorption energy of lithium in MXene/δ-MnO_2 is the highest. As shown in the band structure, MnO_2 is a wide band gap semiconductor with poor electrical conductivity, but after the H–O bonding, it becomes a conductor with significantly increased electron population on the Fermi level, as depicted in the density of states (DOS) (Figure 5c,d). Specifically, the main contribution to the Fermi energy level is from the Ti 3d orbital, which enhances the

electrocatalytic activity of the cathode by replacing the sites of Ti. Additionally, as shown in Figure S17a, in the model wherein one of the Mn is replaced by Ti in MnO_2, the bond length of Mn–O is shorter than that of the Ti–O bond, which is due to the fact that the electronegativity of Ti is not as large as that of Mn. After the substitution, the adsorption energy is enhanced for $Ti_xMn_{1-x}O_2$, which promotes the reaction between CO_2 and Li to form Li_2CO_3. The adsorption energies of different Li with the three cases are shown in Figure S17b, among which the adsorption energy of $Ti_xMn_{1-x}O_2$ is the largest.

4. Conclusions

The stand-alone and binder-free MXene–MnO_2 composite electrode in the field of Li–air batteries was synthesized by vacuum filtration and redox reaction. Based on this self-supporting cathode catalyst, the Ti_3C_2–0.1MnO_2 film-based Li–CO_2 cell can be stably cycled (220 cycles) at a lower overpotential even when operating at a fixed capacity of 1000 mA h g^{-1} at 100 mA g^{-1}. After the pre-activation process, the overpotential of the charge/discharge curve was as low as 0.89 V at the tenth cycle compared with the Ti_3C_2 film and MnO_2 cathode. The excellent electrocatalytic activity performance can be ascribed to the following reasons. First, the high electrical conductivity and porous structure of the MXene–MnO_2 film provide fast electron and ion transport channels during the charging and discharging process. Second, the replacement of Mn by Ti increases the adsorption of lithium ions and facilitates the rapid decomposition of Li_2CO_3. Third, the synergistic effect between the MXene film and MnO_2 exposes more active sites, which in turn increases the capacity of the Li–CO_2 batteries. The pioneering effort of this study is to investigate MXene as a freestanding catalyst for catalytic activity enhancement and discharge product control in Li–CO_2 batteries, which provides a new perspective on the design of catalysts for rechargeable metal-gas batteries.

Notes

The authors declare no competing financial interest.

ACKNOWLEDGMENTS

We greatly acknowledge financial support from the National Natural Science Foundation-Outstanding Youth Foundation (51971194 and 51771162) and Hebei Province Talent Project (A201910002). We would like to express our gratitude to Ministry of Education Yangtze River Scholar Professor Program.

REFERENCES

(1) Cano, Z. P.; Banham, D.; Ye, S.; Hintennach, A.; Lu, J.; Fowler, M.; Chen, Z. Batteries and Fuel Cells for Emerging Electric Vehicle Markets. Nat. Energy 2018, 3, 279−289.

(2) Chen, J.; Zou, K.; Ding, P.; Deng, J.; Zha, C.; Hu, Y.; Zhao, X.; Wu, J.; Fan, J.; Li, Y. Conjugated Cobalt Polyphthalocyanine as the Elastic and Reprocessable Catalyst for Flexible Li-CO2 Batteries. Adv. Mater. 2019, 31, 1805484.

(3) Leskes, M.; Drewett, N. E.; Hardwick, L. J.; Bruce, P. G.; Goward, G. R.; Grey, C. P. Direct Detection of Discharge Products in Lithium-Oxygen Batteries by Solid-State NMR Spectroscopy. Angew. Chem., Int. Ed. 2012, 51, 8560−8563.

(4) Xie, Z.; Zhang, X.; Zhang, Z.; Zhou, Z. Metal-CO2 Batteries on the Road: CO2 from Contamination Gas to Energy Source. Adv. Mater. 2017, 29, 1605891.

(5) Yang, S.; Qiao, Y.; He, P.; Liu, Y.; Cheng, Z.; Zhu, J.-j.; Zhou, H. A Reversible Lithium-CO2 Battery with Ru Nanoparticles as a Cathode Catalyst. Energy Environ. Sci. 2017, 10, 972−978.

(6) Zhao, Z.; Huang, J.; Peng, Z. AchillesQ Heel of Lithium−Air Batteries: Lithium Carbonate. Angew. Chem., Int. Ed. 2018, 130, 3936−3949.

(7) Wang, H.; Xie, K.; You, Y.; Hou, Q.; Zhang, K.; Li, N.; Yu, W.; Loh, K. P.; Shen, C.; Wei, B. Realizing Interfacial Electronic Interaction within ZnS Quantum Dots/N-rGO Heterostructures for Efficient Li-CO2 Batteries. Adv. Energy Mater. 2019, 9, 1901806.

(8) Qiao, Y.; Yi, J.; Guo, S.; Sun, Y.; Wu, S.; Liu, X.; Yang, S.; He, P.; Zhou, H. Li2CO3-free Li−O2/CO2 Battery with Peroxide Discharge Product. Energy Environ. Sci. 2018, 11, 1211−1217.

(9) Qie, L.; Lin, Y.; Connell, J. W.; Xu, J.; Dai, L. Highly Rechargeable Lithium-CO2 Batteries with a Boron-and Nitrogen- Codoped Holey-Graphene Cathode. Angew. Chem., Int. Ed. 2017, 129, 7074−7078.

(10) Lim, H.-K.; Lim, H.-D.; Park, K.-Y.; Seo, D.-H.; Gwon, H.; Hong, J.; Goddard, W. A.; Kim, H.; Kang, K. Toward a Lithium-"Air" Battery: The Effect of CO2 on the Chemistry of a Lithium-Oxygen Cell. J. Am. Chem. Soc. 2013, 135, 9733−9742.

(11) Zhang, Z.; Yang, C.; Wu, S.; Wang, A.; Zhao, L.; Zhai, D.; Ren, B.; Cao, K.; Zhou, Z. Exploiting Synergistic Effect by Integrating Ruthenium-Copper Nanoparticles Highly Co-Dispersed on Graphene as Efficient Air Cathodes for Li-CO2 Batteries. Adv. Energy Mater. 2019, 9, 1802805.

(12) Zhang, Z.; Zhang, Z.; Liu, P.; Xie, Y.; Cao, K.; Zhou, Z. Identification of Cathode Stability in Li−CO2 Batteries with Cu Nanoparticles Highly Dispersed on N-doped Graphene. J. Mater. Chem. A 2018, 6, 3218−3223.

(13) Zhang, Z.; Wang, X.-G.; Zhang, X.; Xie, Z.; Chen, Y.-N.; Ma, L.; Peng, Z.; Zhou, Z. Verifying the Rechargeability of Li-CO2 Batteries on Working Cathodes of Ni Nanoparticles Highly Dispersed on N-Doped Graphene. Adv. Sci. 2018, 5, 1700567.

(14) Ge, B.; Sun, Y.; Guo, J.; Yan, X.; Fernandez, C.; Peng, Q. A Co- Doped MnO2 Catalyst for Li-CO2 Batteries with Low Overpotential and Ultrahigh Cyclability. Small 2019, 15, 1902220.

(15) Zhang, X.; Wang, C.; Li, H.; Wang, X.-G.; Chen, Y.-N.; Xie, Z.; Zhou, Z. High Performance Li-CO2 Batteries with NiO-CNT Cathodes. J. Mater. Chem. A 2018, 6, 2792−2796.

(16) Thoka, S.; Chen, C.-J.; Jena, A.; Wang, F.-M.; Wang, X.-C.; Chang, H.; Hu, S.-F.; Liu, R.-S. Spinel Zinc Cobalt Oxide (ZnCo2O4) Porous Nanorods as a Cathode Material for Highly Durable Li−CO2 Batteries. ACS Appl. Mater. Interfaces 2020, 12, 17353−17363.

(17) Zhang, J.; Kong, N.; Uzun, S.; Levitt, A.; Seyedin, S.; Lynch, P. A.; Qin, S.; Han, M.; Yang, W.; Liu, J.; Wang, X.; Gogotsi, Y.; Razal, J. M. Scalable Manufacturing of Free-Standing Strong Ti3C2Tx MXene Films with Outstanding Conductivity. Adv. Mater. 2020, 32, 2001093.

(18) Ramalingam, V.; Varadhan, P.; Fu, H. C.; Kim, H.; Zhang, D.; Chen, S.; Song, L.; Ma, D.; Wang, Y.; Alshareef, H. N.; He, J. H. Heteroatom-Mediated Interactions between Ruthenium Single Atoms and an MXene Support for Efficient Hydrogen Evolution. Adv. Mater. 2019, 31, 1903841.

(19) Ghidiu, M.; Lukatskaya, M. R.; Zhao, M.-Q.; Gogotsi, Y.; Barsoum, M. W. Conductive Two-dimensional Titanium Carbide 'clay' with High Volumetric Capacitance. Nature 2014, 516, 78−81.

(20) Zhou, Y.; Maleski, K.; Anasori, B.; Thostenson, J. O.; Pang, Y.; Feng, Y.; Zeng, K.; Parker, C. B.; Zauscher, S.; Gogotsi, Y.; Glass, J. T.; Cao, C. Ti3C2Tx MXene-Reduced Graphene Oxide Composite Electrodes for Stretchable Supercapacitors. ACS Nano 2020, 14, 3576−3586.

(21) Zhang, Y.; Mu, Z.; Lai, J.; Chao, Y.; Yang, Y.; Zhou, P.; Li, Y.; Yang, W.; Xia, Z.; Guo, S. MXene/Si@SiOx@C Layer-by-Layer Superstructure with Autoadjustable Function for Superior Stable Lithium Storage. ACS Nano 2019, 13, 2167−2175.

(22) Zou, G.; Guo, J.; Liu, X.; Zhang, Q.; Huang, G.; Fernandez, C.; Peng, Q. Hydrogenated Core-Shell MAX@K2Ti8O17 Pseudocapaci- tance with Ultrafast Sodium Storage and Long-Term Cycling. Adv. Energy Mater. 2017, 7, 1700700.

(23) Benchakar, M.; Bilyk, T.; Garnero, C.; Loupias, L.; Morais, C.; Pacaud, J.; Canaff, C.; Chartier, P.; Morisset, S.; Guignard, N.; Mauchamp, V.; Célérier, S.; Habrioux, A. MXene Supported Cobalt Layered Double Hydroxide Nanocrystals:Facile Synthesis Route for a Synergistic Oxygen Evolution Reaction Electrocatalyst. Adv. Mater. Interfaces 2019, 6, 1901328.

(24) Zhang, J.; Zhao, Y.; Guo, X.; Chen, C.; Dong, C.-L.; Liu, R.-S.; Han, C.-P.; Li, Y.; Gogotsi, Y.; Wang, G. Single Platinum Atoms Immobilized on an MXene as an Efficient Catalyst for the Hydrogen Evolution Reaction. Nat. Catal. 2018, 1, 985−992.

(25) Yuan, W.; Cheng, L.; An, Y.; Wu, H.; Yao, N.; Fan, X.; Guo, X. MXene Nanofibers as Highly Active Catalysts for Hydrogen Evolution Reaction. ACS Sustainable Chem. Eng. 2018, 6, 8976−8982.

(26) Lukatskaya, M. R.; Kota, S.; Zhao, M.-Q.; Shpigel, N.; Levi, M. D.; Halim, J.; Taberna, P.-L.; Barsoum, M. W.; Simon, P.; Gogotsi, Y. Ultra-high-rate Pseudocapacitive Energy Storage in Two-dimensional Transition Metal Carbides. Nat. Energy 2017, 2, 17105.

(27) Tang, J.; Yi, W.; Zhong, X.; Zhang, C.; Xiao, X.; Pan, F.; Xu, B. Laser Writing of the Restacked Titanium Carbide MXene for High Performance Supercapacitors. Energy Storage Mater. 2020, 32, 418− 424.

(28) Chen, J.; Yuan, X.; Lyu, F.; Zhong, Q.; Hu, H.; Pan, Q.; Zhang, Q. Integrating MXene Nanosheets with Cobalt-tipped Carbon Nanotubes for an Efficient Oxygen Reduction Reaction. J. Mater. Chem. A 2019, 7, 1281−1286.

(29) Hohenberg, P.; Kohn, W. Inhomogeneous Electron Gas. Phys. Rev. 1964, 136, B864−B871.

(30) Kohn, W.; Sham, L. J. Self-consistent Equations Including Exchange and Correlation Effects. Phys. Rev. 1965, 140, A1133− A1138.

(31) Kresse, G.; Furthmüller, J. Efficiency of ab-initio Total Energy Calculations for Metals and Semiconductors Using a Plane-wave Basis Set. Comput. Mater. Sci. 1996, 6, 15−50.

(32) Perdew, J. P.; Wang, Y. Accurate and Simple Analytic Representation of the Electron-gas Correlation Energy. Phys. Rev. B: Condens. Matter Mater. Phys. 1996, 45, 13244−13249.

(33) Li, T.; Yao, L.; Liu, Q.; Gu, J.; Luo, R.; Li, J.; Yan, X.; Wang, W.; Liu, P.; Chen, B.; Zhang, W.; Abbas, W.; Naz, R.; Zhang, D. Fluorine-Free Synthesis of High-Purity Ti3C2Tx (T=OH, O) via Alkali Treatment. Angew. Chem., Int. Ed. 2018, 57, 6115−6119.

(34) Liang, X.; Hart, C.; Pang, Q.; Garsuch, A.; Weiss, T.; Nazar, L. F. A Highly Efficient Polysulfide Mediator for Lithium−sulfur Batteries. Nat. Commun. 2015, 6, 5682.

(35) Zou, G.; Ge, B.; Zhang, H.; Zhang, Q.; Fernandez, C.; Li, W.; Huang, J.; Peng, Q. Self-Reductive Synthesis of MXene/ Na0.55Mn1.4Ti0.6O4 Hybrids for High-performance Symmetric Lithium ion Batteries. J. Mater. Chem. A 2019, 7, 7516−7525.

(36) Lei, D.; Ma, S.; Lu, Y.; Liu, Q.; Li, Z. High-Performance Li-CO2 Batteries with α-MnO2/CNT Cathodes. J. Electron. Mater. 2019, 48, 4653−4659.

(37) Dong, H.; Jin, C.; Gao, Y.; Xiao, X.; Li, K.; Tang, P.; Li, X.; Yang, S. Nitrogen and Sulfur co-doped Three-dimensional Gra- phene@NiO Composite as Cathode Catalyst for the Li−O2 and Li−CO2 Batteries. Mater. Res. Express 2019, 6, 115616.

(38) Jena, A.; Hsieh, H. C.; Thoka, S.; Hu, S. F.; Chang, H.; Liu, R. S. Curtailing the Overpotential of Li-CO2 Batteries with Shape- Controlled Cu2O as Cathode: Effect of Illuminating the Cathode. ChemSusChem 2020, 13, 2719−2725.

(39) Ma, W.; Lu, S.; Lei, X.; Liu, X.; Ding, Y. Porous Mn2O3 Cathode for Highly Durable Li−CO2 Batteries. J. Mater. Chem. A 2018, 6, 20829−20835.

(40) Tang, Z.; Yuan, M.; Zhu, H.; Zeng, G.; Liu, J.; Duan, J.; Chen, Z. Promoting the Performance of Li-CO2 Batteries via Constructing Three-Dimensional Interconnected K+ Doped MnO2 Nanowires Networks. Front. Chem. 2021, 9, 670612.

(41) Liu, L.; Zhang, L.; Wang, K.; Wu, H.; Mao, H.; Li, L.; Sun, Z.; Lu, S.; Zhang, D.; Yu, W.; Ding, S. Understanding the Dual-Phase Synergy Mechanism in Mn2O3-Mn3O4 Catalyst for Efficient Li-CO2 Batteries. ACS Appl. Mater. Interfaces 2020, 12, 33846−33854.

(42) Jiang, C.; Zhang, Y.; Zhang, M.; Ma, N.-N.; Gao, G.-K.; Wang, J.-H.; Zhang, M.-M.; Chen, Y.; Li, S.-L.; Lan, Y.-Q. Exfoliation of Covalent Organic Frameworks into MnO2-loaded Ultrathin Nano- sheets as Efficient Cathode Catalysts for Li-CO2 Batteries. Cell Rep. Phys. Sci. 2021, 2, 100392.

(43) Wang, C.; Lu, Y.; Lu, S.; Ma, S.; Zhu, X.; Li, Z.; Liu, Q. Boosting Li-CO2 battery Performances by Engineering Oxygen Vacancy on NiO Nanosheets Array. J. Power Sources 2021, 495, 229782.

(44) Li, S.; Liu, Y.; Zhou, J.; Hong, S.; Dong, Y.; Wang, J.; Gao, X.; Qi, P.; Han, Y.; Wang, B. Monodispersed MnO Nanoparticles in Graphene-an Interconnected N-doped 3D Carbon Framework as a Highly Efficient Gas Cathode in Li−CO2 Batteries. Energy Environ. Sci. 2019, 12, 1046−1054.

Supporting Information

Freestanding MXene-MnO_2 Films for Li-CO_2 Cathodes with Low Overpotential and Long-term Cycling

*Yangyang Wang, Xue Wang, Bingcheng Ge, Jianxin Guo, Carlos Fernandez, Qiuming Peng**

Dr. Yangyang Wang, Xue Wang, Bingcheng Ge, Prof. Qiuming Peng

CENC, State Key Laboratory of Metastable Materials Science and Technology,

Yanshan University, Qinhuangdao 066004, China

E-mail: pengqiuming@ysu.edu.cn

Dr. Jianxin Guo,

Hebei Provincial Key Lab of Optoelectronic Information Materials, College of Physics Science and Technology, Hebei University, Baoding, 071002, China.

Dr. Carlos Fernandez

School of Pharmacy and life sciences, Robert Gordon University, Aberdeen,

AB107GJ, United Kingdom

Table S1. Fitting parameters of EIS curves of the Ti_3C_2-0.05MnO_2 film sample in terms of fitting circuits.

Samples	states	R_e	R_f	Q_1		R_{ct}	Q_2	
		(Ω)	(Ω)	Y	n	(Ω)	Y	n
Ti_3C_2-0.05MnO_2	Pristine	27.3	105.9	2.5×10^{-4}	0.82	136.4	2.1×10^{-5}	0.66
	1^{st} Discharge	19.74	4205	1.3×10^{-4}	0.8	679.8	1.0×10^{-7}	0.80
	1^{st} Charge	30.61	2420	7.6×10^{-5}	1.0	336.1	2.9×10^{-6}	0.78

Table S2. Fitting parameters of EIS curves of the Ti_3C_2-0.2MnO_2 film sample in terms of fitting circuits.

Samples	states	R_e (Ω)	R_f (Ω)	Q1		R_{ct} (Ω)	Q2	
				Y	n		Y	n
Ti_3C_2-0.2 MnO_2	Pristine	30.25	333.1	4.3×10^{-4}	0.89	108.9	5.8×10^{-6}	0.83
	1st Discharge	25.36	56.7	6.2×10^{-3}	0.28	277.3	1.01×10^{-5}	0.65
	1st Charge	33.59	187.6	7.3×10^{-3}	0.8	123.1	3.4×10^{-5}	0.8

Table S3. Fitting parameters of EIS curves of the Ti_3C_2-0.1MnO_2 film、 Ti_3C_2 film and MnO_2 sample in terms of fitting circuits, respectively.

Samples	states	R_e (Ω)	R_f (Ω)	Q_1		R_{ct} (Ω)	Q_2	
				Y	n		Y	n
Ti_3C_2-0.1 MnO_2 film	Pristine	26.03	769.4	5.1×10^{-4}	0.89	116	5.1×10^{-6}	0.83
	1st Discharge	24.65	1306	1.6×10^{-3}	0.67	270.3	1.02×10^{-5}	0.69
	1st Charge	13.76	34.03	3.6×10^{-3}	0.8	91.59	1.3×10^{-4}	0.50
Ti_3C_2 film	Pristine	3.97	10.47	6.1×10^{-4}	0.8	577.9	1.4×10^{-7}	0.77
	1st Discharge	38.4	3271	1.2×10^{-5}	0.6	36.7	2.0×10^{-8}	0.9
	1st Charge	0.01	68.7	2.0×10^{-4}	0.8	1461	1.0×10^{-7}	0.8
MnO_2	Pristine	20.32	2.2×10^{13}	1.0×10^{-2}	0.8	147	2.4×10^{-5}	0.8
	1st Discharge	18.5	7.6×10^{5}	1.6×10^{-3}	0.82	363.4	2.4×10^{-5}	0.61
	1st Charge	26.56	1.763	1.6×10^{-4}	0.92	193.2	1.63×10^{-5}	0.72

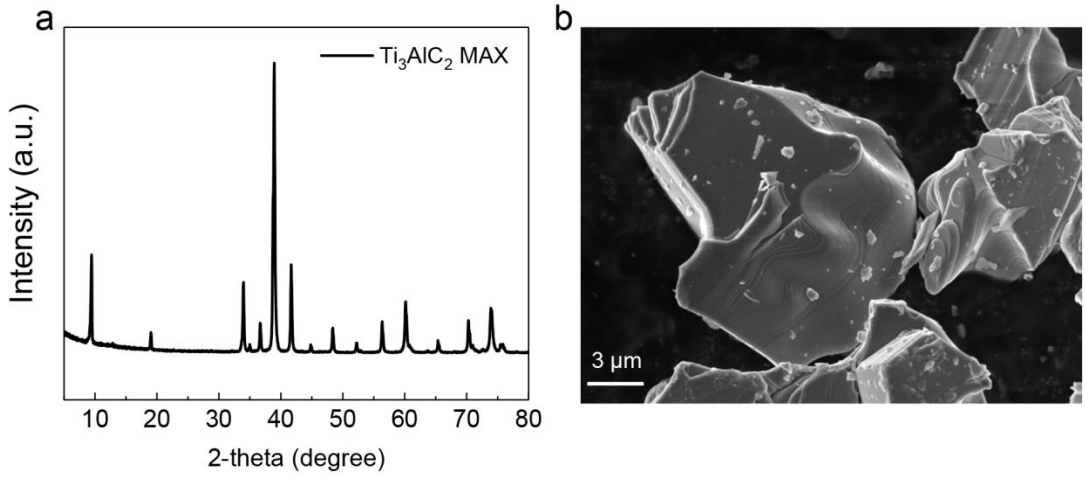

Figure S1. a) XRD pattern and b) SEM image of the MAX phase Ti_3AlC_2

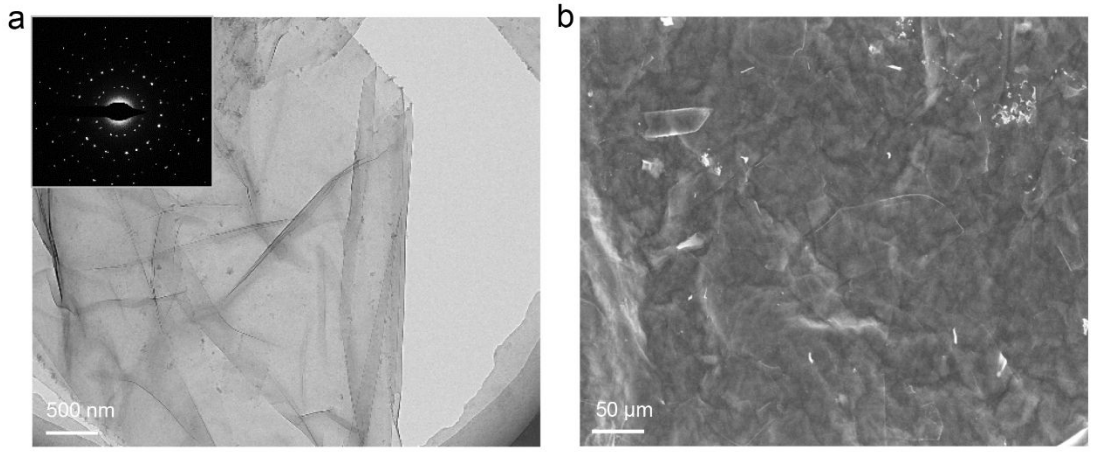

Figure S2**.** a) TEM image of MXene nanosheets. The inset is the selected area electron diffraction pattern of MXene. b) Top-view SEM image of Ti_3C_2 film.

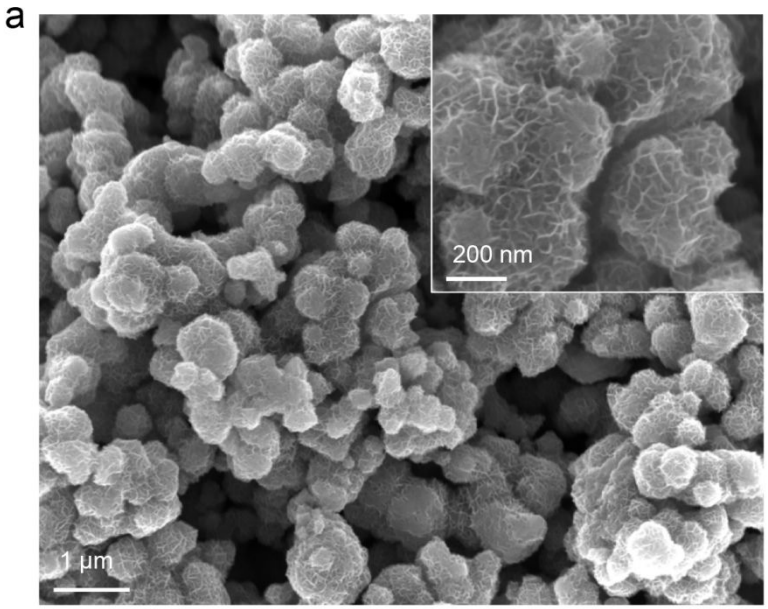

Figure S3. a) SEM image of MnO_2. The inset corresponds to its local high-magnification image.

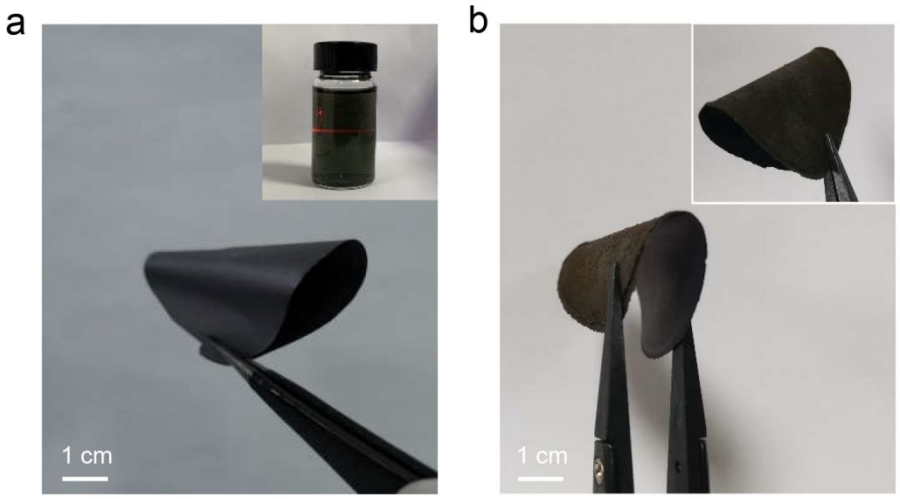

Figure S4. a) Optical photographs of curving MXene film. The inset is tyndall effect of laser irradiation. b) Optical photographs of Ti_3C_2-0.1MnO_2 film.

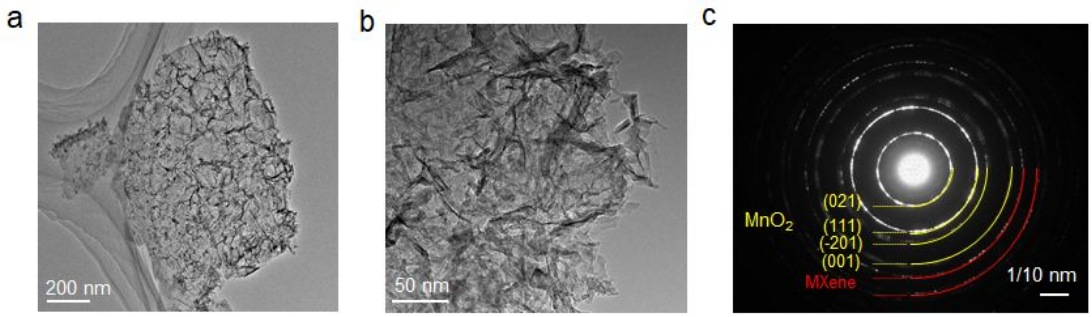

Figure S5. a-b) TEM, and c) the selected area electron diffraction pattern of Ti_3C_2-$0.1MnO_2$ film, respectively.

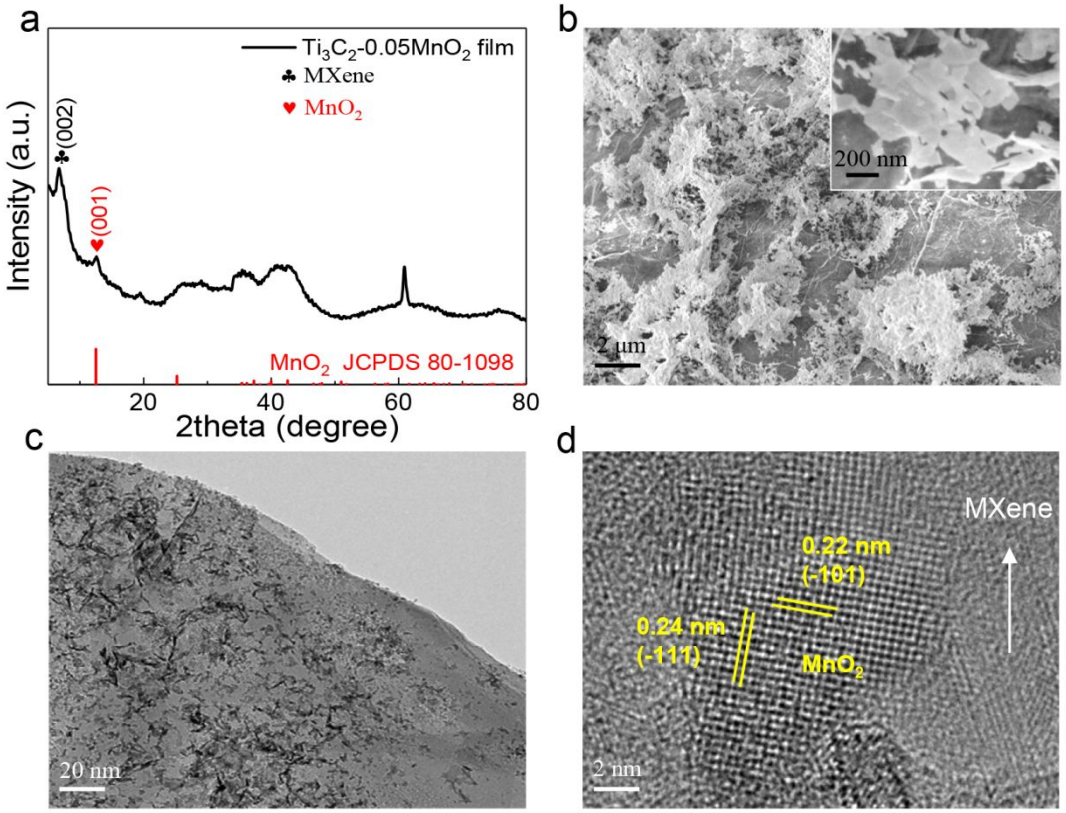

Figure S6. a) XRD pattern and b) SEM, c) TEM, d) HRTEM image of Ti_3C_2-0.05MnO_2 film respectively. The inset of b) is local high-magnification image of Ti_3C_2-0.05MnO_2 film.

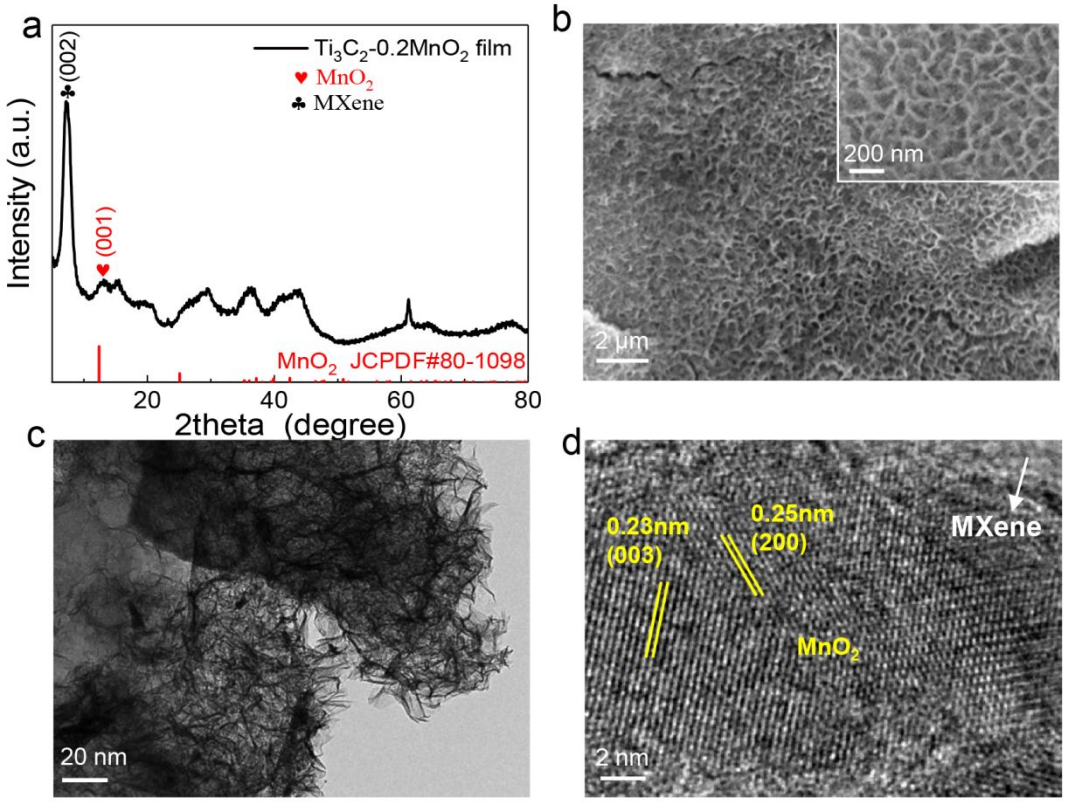

Figure S7. a) XRD pattern and b) SEM, c) TEM, d) HRTEM image of Ti_3C_2-0.2MnO_2 film respectively. The inset of b) is local high-magnification image of Ti_3C_2-0.2MnO_2 film.

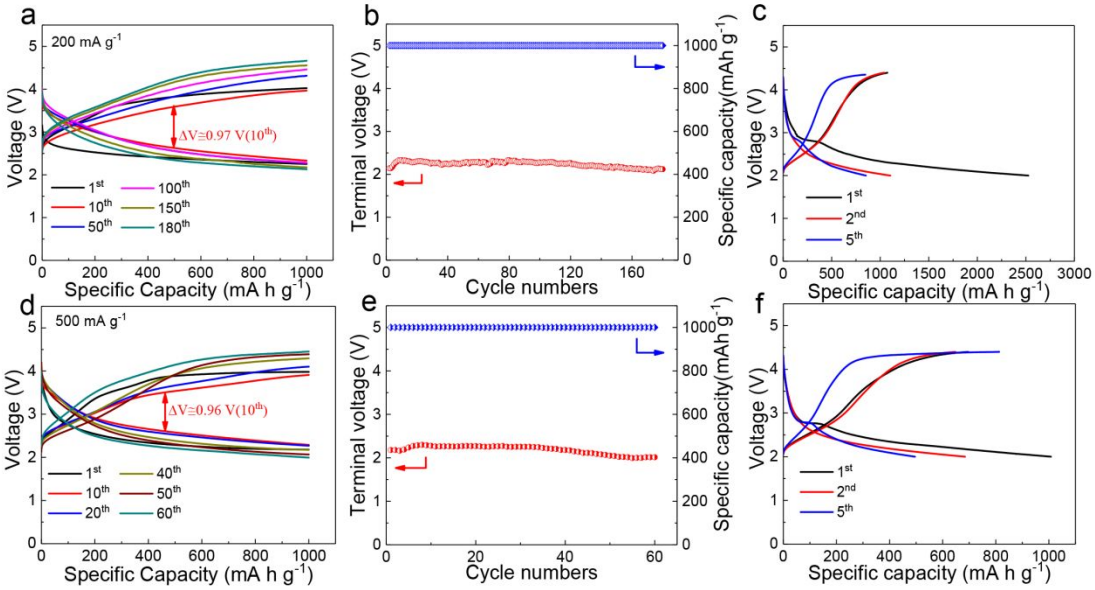

Figure S8. a) Discharge-charge cycling stability of Ti_3C_2-0.1MnO_2 film at 200 mA g^{-1} with a cut-off capacity of 1000 mA h g^{-1}. b) Cycling stability and terminal discharge-charge voltages of Ti_3C_2-0.1MnO_2 film cathode at 200 mA g^{-1} with a limited capacity of 1000 mA h g^{-1}. c) The first charge/discharge properties of Ti_3C_2-0.1MnO_2 film under 200 mA g^{-1}. d) Discharge-charge cycling stability of Ti_3C_2-0.1MnO_2 film at 500 mA g^{-1} with a cut-off capacity of 1000 mA h g^{-1}. e) Cycling stability and terminal discharge-charge voltages of Ti_3C_2-0.1MnO_2 film cathode at 500 mA g^{-1} with a limited capacity of 1000 mA h g^{-1}. f) The first charge/discharge properties of Ti_3C_2-0.1MnO_2 film under 500 mA g^{-1}.

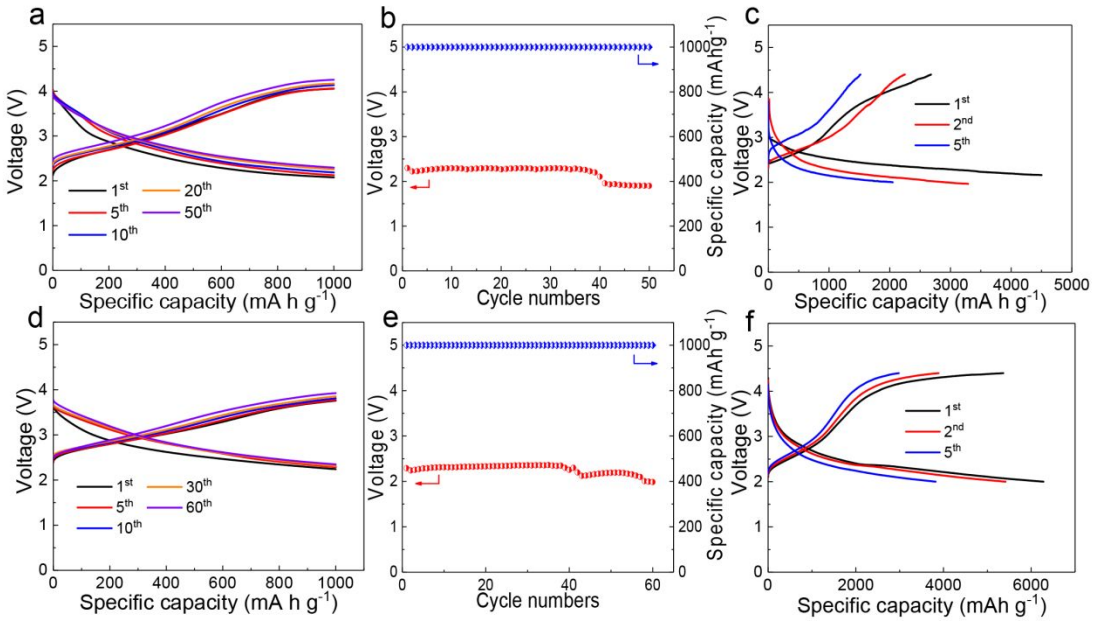

Figure S9. a) Discharge-charge cycling stability of Ti_3C_2-0.05MnO_2 film at 100 mA g^{-1} with a cut-off capacity of 1000 mA h g^{-1}. b) Cycling stability and terminal discharge-charge voltages of Ti_3C_2-0.05MnO_2 film cathode at 100 mA g^{-1} with a limited capacity of 1000 mA h g^{-1}. c) The first charge/discharge properties of Ti_3C_2-0.05MnO_2 film under 100 mA g^{-1}. d) Discharge-charge cycling stability of Ti_3C_2-0.2MnO_2 film at 100 mA g^{-1} with a cut-off capacity of 1000 mA h g^{-1}. e) Cycling stability and terminal discharge-charge voltages of Ti_3C_2-0.2MnO_2 film cathode at 100 mA g^{-1} with a limited capacity of 1000 mA h g^{-1}. f) The first charge/discharge properties of Ti_3C_2-0.2MnO_2 film under 100 mA g^{-1}.

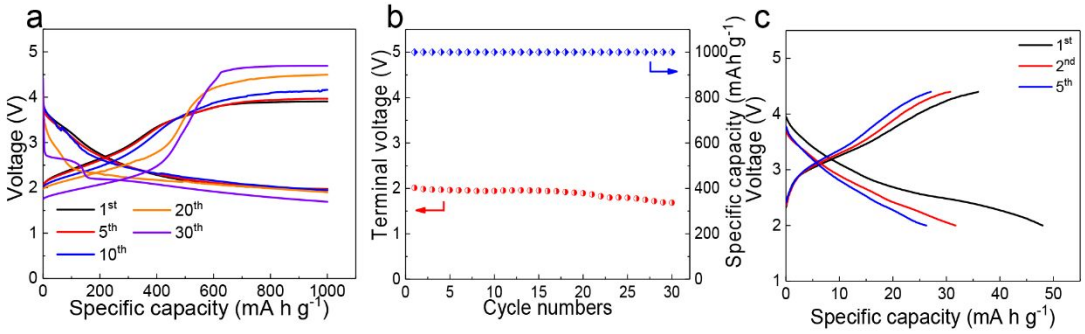

Figure S10. a) Discharge-charge cycling stability of Ti_3C_2 film at 100 mA g^{-1} with a cut-off capacity of 1000 mA h g^{-1}. b) Cycling stability and terminal discharge-charge voltages of Ti_3C_2 film cathode at 100 mA g^{-1} with a limited capacity of 1000 mA h g^{-1}. c) The first charge/discharge properties of Ti_3C_2 film under 100 mA g^{-1}.

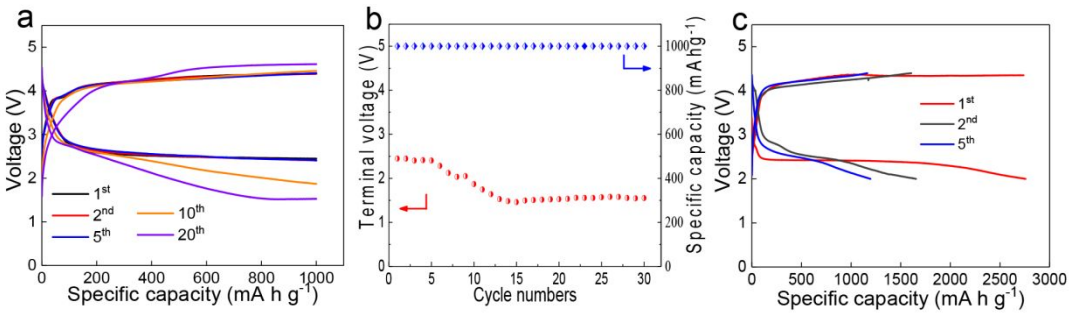

Figure S11. a) Discharge-charge cycling stability of MnO_2 at 100 mA g^{-1} with a cut-off capacity of 1000 mA h g^{-1}. b) Cycling stability and terminal discharge-charge voltages of MnO_2 cathode at 100 mA g^{-1} with a limited capacity of 1000 mA h g^{-1}. c) The first charge/discharge properties of MnO_2 under 100 mA g^{-1}.

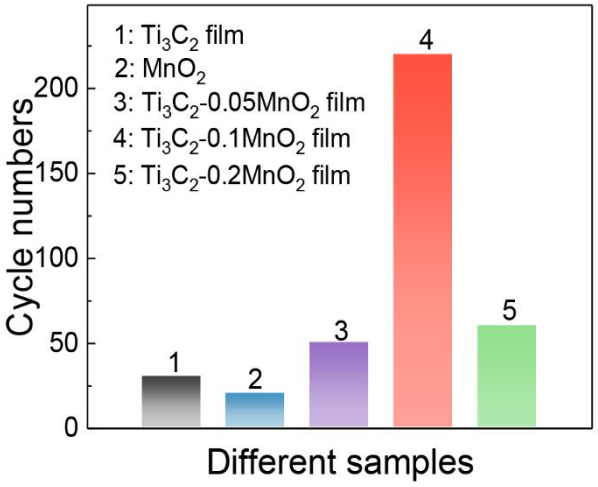

Figure S12. The cycle numbers of Li-CO_2 batteries with different samples.

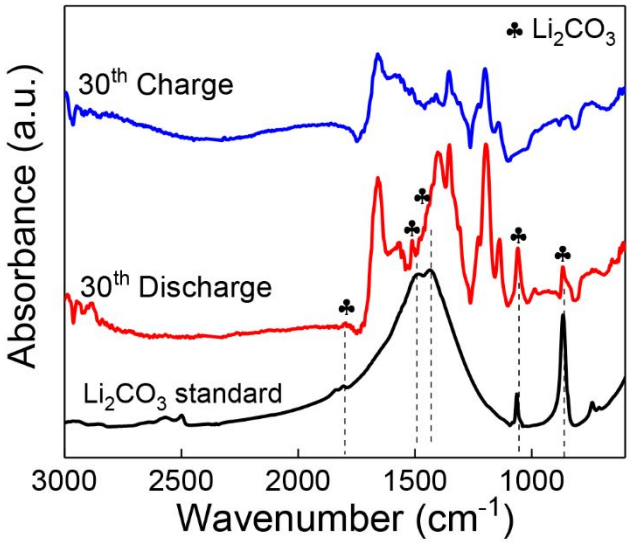

Figure S13. FTIR of the MXene-MnO_2 film electrodes at different states.

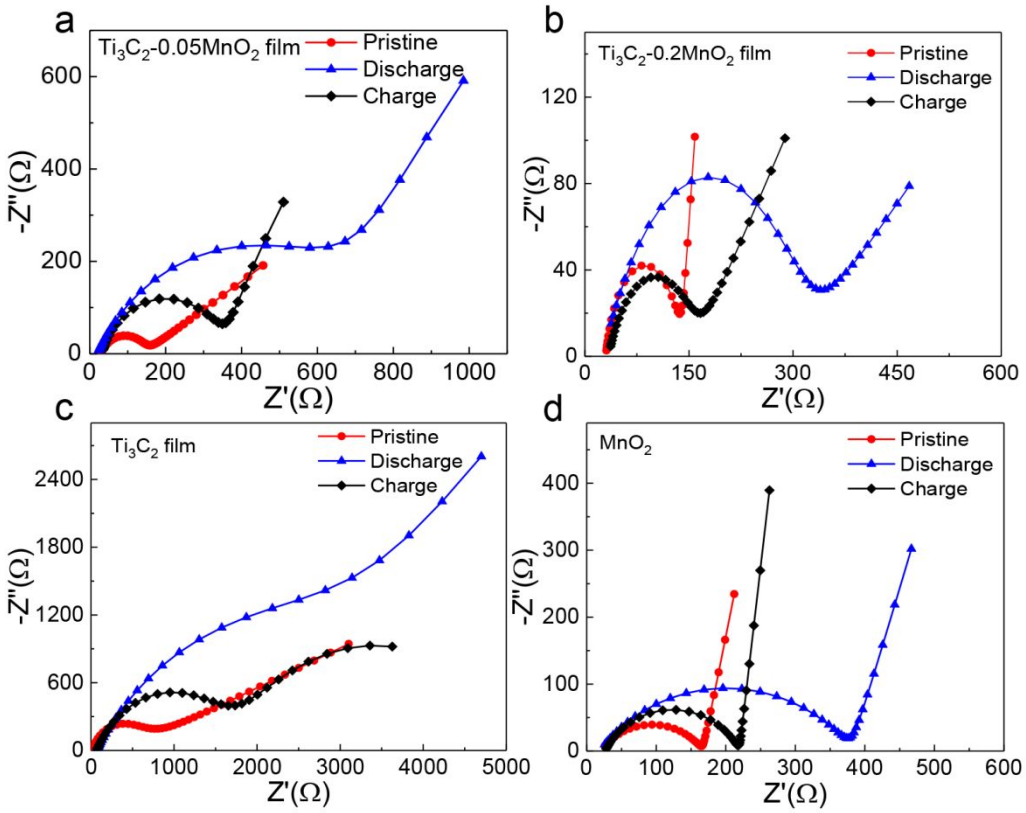

Figure S14. The electrochemical impedance spectroscopy (EIS) determined the impedance of the battery under three states of electrodes with a) Ti_3C_2-0.05MnO_2 film, b) Ti_3C_2-0.2MnO_2 film, c) Ti_3C_2 film, d) MnO_2 respectively.

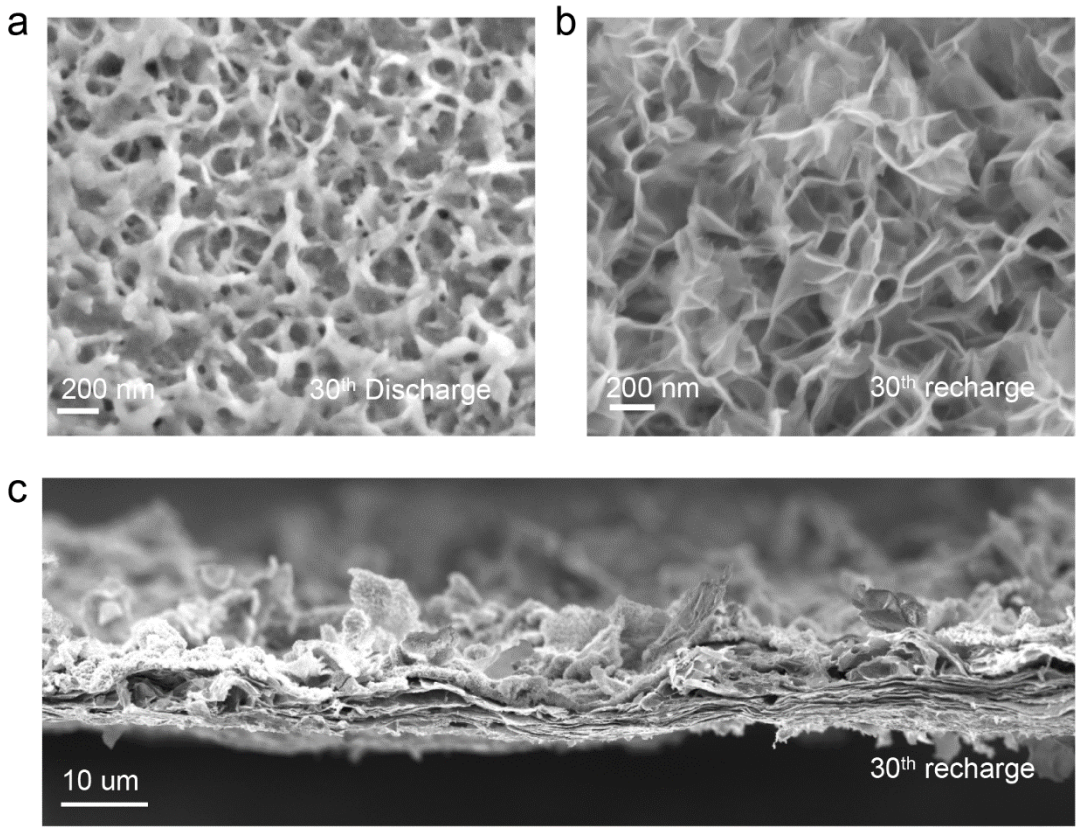

Figure S15. SEM images of the Ti_3C_2-0.1MnO_2 film based cathode in different: top-view SEM (a) 30th discharge, (b) 30th recharge, (c) cross-sectional SEM 30th recharge.

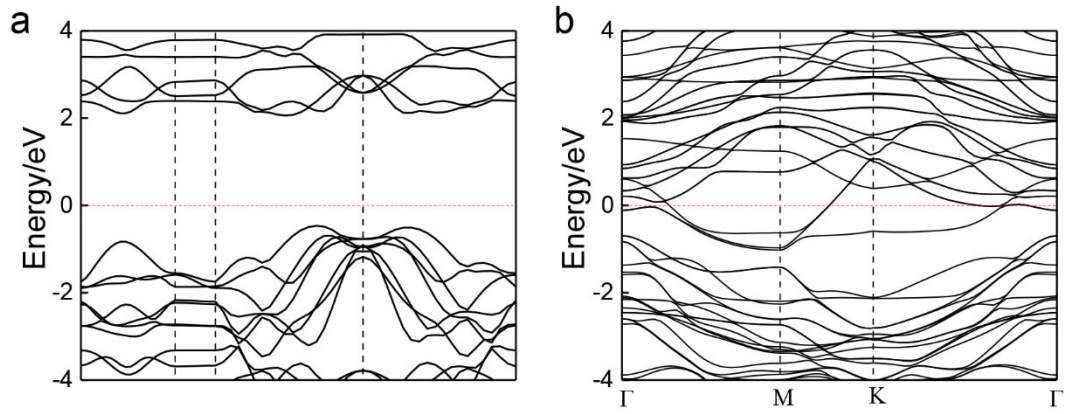

Figure S16. Band structures of δ-MnO_2 a) and MXene/δ-MnO_2 b), respectively.

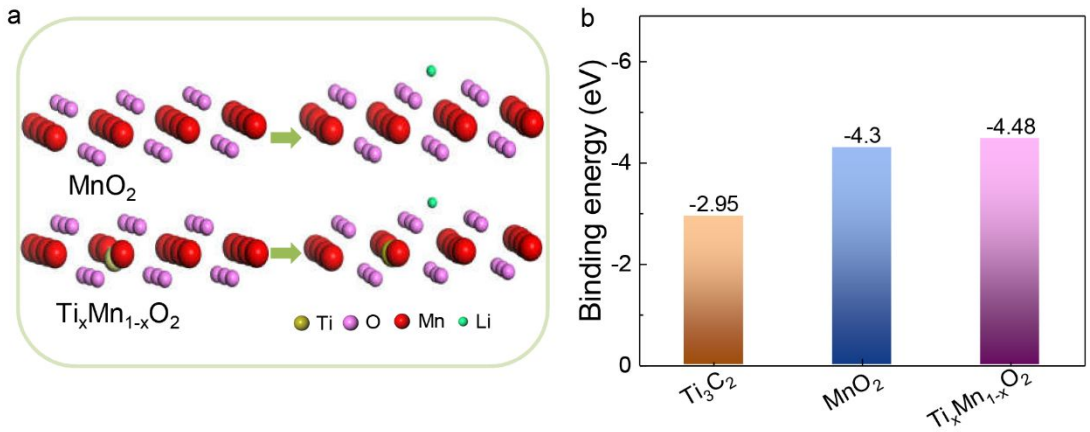

Figure S17 a) Schematic model for adsorption of lithium in a) MnO_2, $Ti_xMn_{1-x}O_2$, respectively. b) The adsorption energy of lithium in Ti_3C_2, MnO_2, $Ti_3C_2O_2$ (001), $Ti_xMn_{1-x}O_2$, respectively.